



Metal oxide top layer as an interfacial promoter on a $\text{ZnIn}_2\text{S}_4/\text{TiO}_2$ heterostructure photoanode for enhanced photoelectrochemical performance

Mahadeo A. Mahadik, Pravin S. Shinde, Min Cho*, Jum Suk Jang*

Division of Biotechnology, Advanced Institute of Environmental and Bioscience, College of Environmental and Bioresource Sciences, Chonbuk National University, Iksan 570-752, Republic of Korea

ARTICLE INFO

Article history:

Received 9 September 2015

Received in revised form

26 November 2015

Accepted 1 December 2015

Available online 2 December 2015

Keywords:

Metal oxide

ZnIn_2S_4 nanosheet

TiO_2 nanorod

Hydrogen production

Heterostructure photoanode

ABSTRACT

We designed metal oxide coated $\text{ZnIn}_2\text{S}_4/\text{TiO}_2$ (ZT) heterostructure photoanodes for enhanced photoelectrochemical performance via hydrothermal and dip-coating methods. The effects of thin metal oxide coating layers, such as TiO_2 , Al_2O_3 , and SiO_2 , on the structural, morphological, optical, and photoelectrocatalytic activity of ZT photoanodes were investigated in detail. The metal oxide coating layers significantly enhanced the photoelectrochemical performance of ZT in the following order: $\text{SiO}_2/\text{ZT} > \text{Al}_2\text{O}_3/\text{ZT} > \text{TiO}_2/\text{ZT} > \text{ZT}$, all at pH 11.5 under simulated one sun illumination. A two-fold boost in the photocurrent density of ZT was recorded after a surface coating of a thin SiO_2 layer among the studied metal oxide layers. The charge transfer resistance measured from the electrochemical impedance spectroscopy (EIS) analysis was less for the SiO_2/ZT photoanode, indicating enhanced charge separation between the oxide surface layer and electrolyte. The enhanced photoelectrochemical performance due to the thin SiO_2 coating was attributed to the improved interface properties that led to the effective charge transfer processes in the vicinity of the electrolyte.

© 2015 Elsevier B.V. All rights reserved.

1. Introduction

Due to the rapid depletion of fossil fuels, the development of renewable energies based on cheap and abundantly available sources is in high demand. The conversion of solar energy into chemical energy (e.g., methane, hydrogen (H_2), methanol) is considered to be one of the most promising approaches to solving environmental and energy demand problems for the future [1]. Increasing attention has been paid to H_2 for developing renewable energy technologies. Hydrogen is the most abundant element and an important chemical reagent in chemical industries. However, due to the emission of large amounts of H_2S from chemical industries, it is now a global threat to the environment. Photocatalysts are a promising candidate for photo-cleavage of H_2S to H_2 , which is seen as a form of recyclable clean energy [2]. Since the first report on water splitting using TiO_2 , semiconductor-based photocatalysis to produce hydrogen energy has been receiving a lot of attention [3]. There are several metal oxide semiconductors with suitable band structures that have already been developed

for hydrogen production [4,5]. These semiconductor catalysts are only active toward UV light, which only absorbs approximately 4% of solar light in the solar spectrum. Hence, the current research explores visible light-driven photocatalysts covering a wide solar spectrum [6]. Several efforts have been made, such as doping foreign elements, along with other potentially effective routes, which include heterostructure and co-catalysis [7–10]. Among the various routes that one can take to improve the photoelectrocatalytic response of semiconductor photoelectrodes, the integration of semiconductors with relative band positions is beneficial for band gap narrowing and expanding the light response to the visible light range. Such band gap tuning can facilitate photo-generated charge separation, which provides a longer carrier lifetime [11]. The shape and size of nanoscale semiconductors may exhibit significant influence on their optoelectronic properties and device performance [12]. Recently, ternary sulphide materials of type AB_2X_4 ($\text{A}=\text{Cu}$, Ag , Zn , Cd ; $\text{B}=\text{Al}$, Ga , In ; $\text{X}=\text{S}$, Se , Te) have attracted attention because of their fascinating nanoscale morphology, as well as their tunable electronic and optical properties, making them useful for different applications [13]. Among these ternary chalcogenides, ZnIn_2S_4 , with a band gap (2.34–2.48 eV) suitable for the visible light region and chemical stability, has attracted considerable attention for hydrogen production from water under visible light irradiation

* Corresponding authors. Fax: +82 63 850 0834.

E-mail addresses: cho317@jbnu.ac.kr (M. Cho), jangs75@jbnu.ac.kr (J.S. Jang).

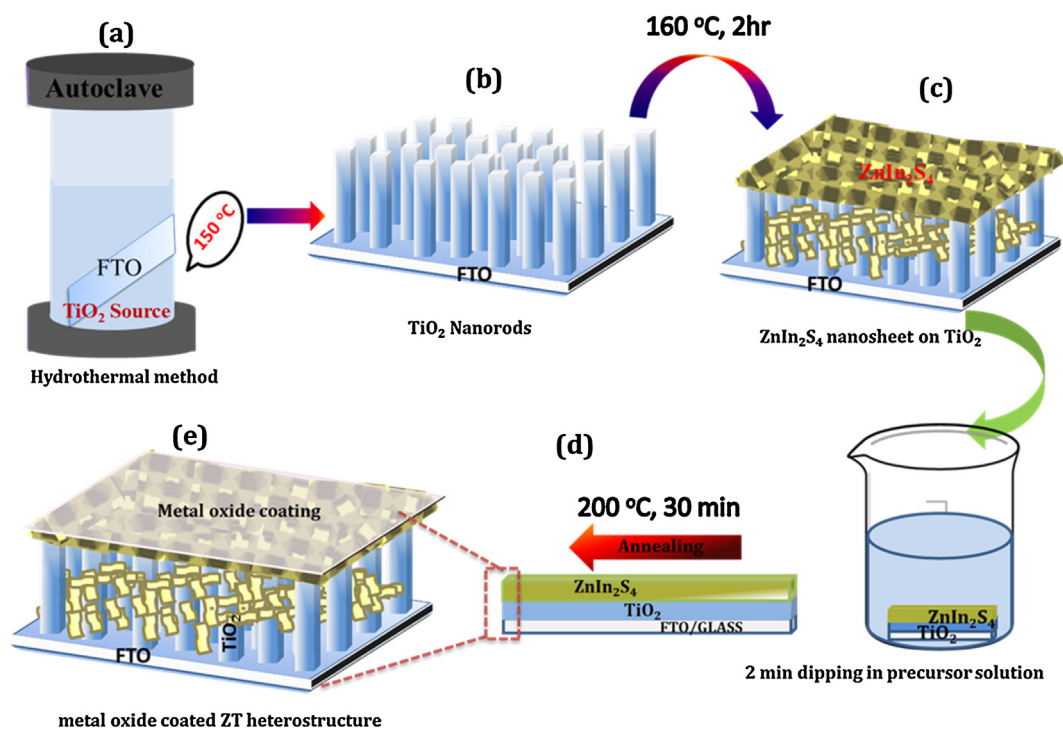


Fig. 1. Schematic of (a–c) the hydrothermal synthesis of TiO_2 and ZT on FTO, and (d,e) fabrication of the metal oxide-coated ZT/FTO heterostructured photoanode.

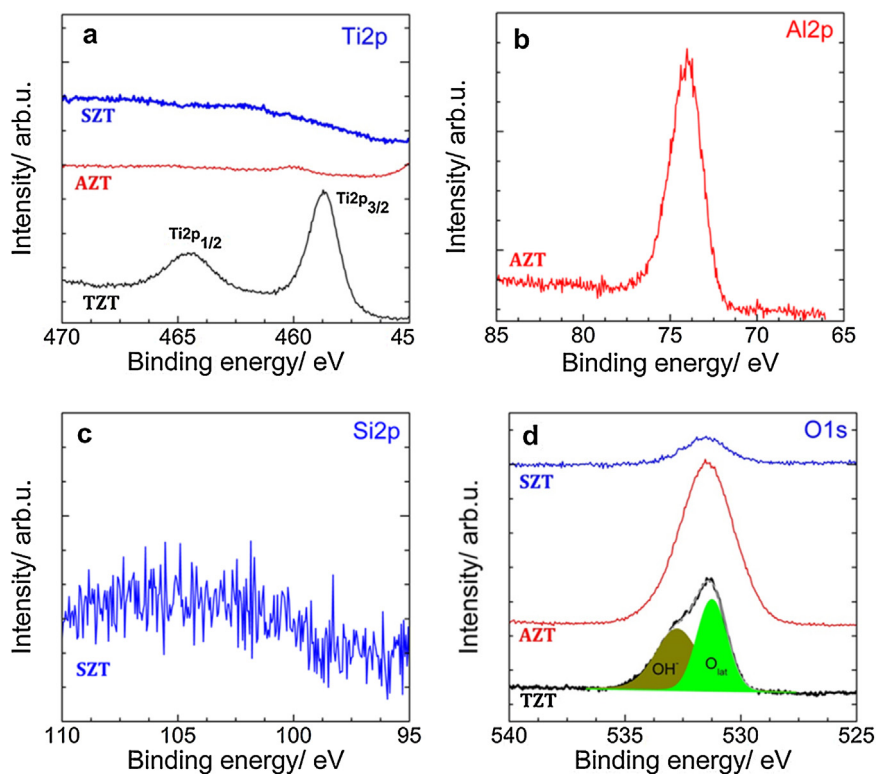


Fig. 2. High-resolution XPS spectra of metal oxide-coated ZT electrodes: (a–d) $\text{Ti}2p$, $\text{Al}2p$, $\text{Si}2p$, and $\text{O}1s$.

[14]. Considering the importance of visible light-active photocatalysts, the $\text{ZnIn}_2\text{S}_4/\text{TiO}_2$ (termed as ZT) heterostructure was reported to significantly promote the photoelectrochemical properties of a TiO_2 photoanode, as its conduction band edge is more negative than that of TiO_2 [15]. However, the efficiency of such heterostructures is low, and a newly designed architecture is required to enhance

the efficiency for the development of a photoanode. Alternatively, metal oxides, such as Fe_2O_3 , TiO_2 , Al_2O_3 , and SiO_2 , have been used as a top layer coating on transition metal oxide semiconductors to enhance the photoelectrocatalytic performance. These coating materials act as a passivation layer that stabilizes the surface defects, monitors the interfacial charge transfer processes at

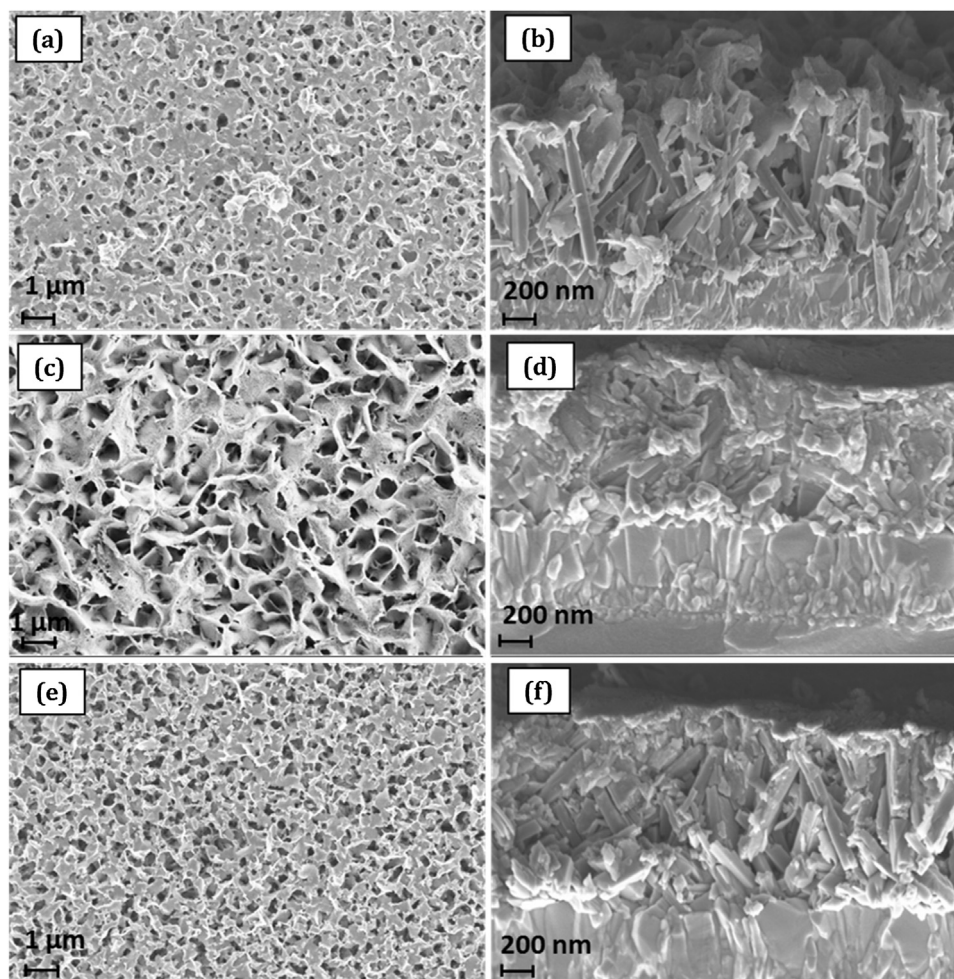


Fig. 3. SEM images of the surface view (a, c, and e), and cross-section (b, d, and f) of TZT, AZT, and SZT thin films, respectively.

the semiconductor/solution interface, and reduces the recombination of charge carriers [16–19]. Such a top metal oxide passivation layer has been employed in many applications, such as solar cells and water splitting. Even though the top layer has not shown the same effects in all cases, metal oxide coatings on transition metal oxide photoanodes have shown promising results for $\text{Al}_2\text{O}_3/\text{Fe}_2\text{O}_3$, $\text{TiO}_2/\text{Cu}_2\text{O}$, and $\text{SiO}_2/\text{TiO}_2$ heterostructure systems in water oxidation. However, there are no reports on the application of metal oxide coated sulfide or chalcogenide architecture photoanodes to enhance the photoelectrochemical activity and stability.

We designed, for the first time, metal oxide-coated $\text{ZnIn}_2\text{S}_4/\text{TiO}_2$ (ZT) heterostructure photoanodes for enhanced photoelectrochemical performance via hydrothermal and dip-coating methods. Although there are few reports on the preparation of ZnIn_2S_4 and ZT, the metal oxide layer coated ZT architecture on the FTO substrate has not been reported previously. TiO_2 , Al_2O_3 and SiO_2 layers were prepared on the surface of pre-synthesized ZT by a dip-coating method and the resulting photoelectrochemical performances were evaluated under solar light irradiations. The SiO_2 -coated ZT photoanode exhibited enhancements in the photocurrent response as compared to that of pristine ZT, and TiO_2 , Al_2O_3 -coated ZT. SiO_2 was a more efficient interfacial promoting layer than TiO_2 and Al_2O_3 due to the interfacial electron transfer between the photoanode and electrolyte and the suppression of recombination of photo-induced charge carriers; this leads to enhanced photoelectrochemical performance. Additionally, the

photoelectrocatalytic activity for hydrogen evolution over SiO_2/ZT was investigated.

2. Experimental

2.1. Reagents and chemicals

The titanium(IV) butoxide ($\text{Ti}(\text{OCH}_2\text{CH}_2\text{CH}_2\text{CH}_3)_4$), hydrochloric acid, zinc sulfate heptahydrate ($\text{ZnSO}_4 \cdot 7\text{H}_2\text{O}$), indium chloride tetrahydrate ($\text{InCl}_3 \cdot 4\text{H}_2\text{O}$), thioacetamide (CH_3CSNH_2), aluminium isopropoxide ($\text{C}_9\text{H}_{21}\text{O}_3\text{Al}$), and tetraethyl orthosilicate ($\text{SiC}_8\text{H}_{20}\text{O}_4$) were the analytical reagents and used as received without further purification.

2.2. Preparation of TiO_2 , Al_2O_3 , and SiO_2 top layers on the ZT heterostructure photoelectrode

Firstly, TiO_2 nanorods were synthesized on FTO by a facile hydrothermal process according to the literature [20]. Prior to the deposition, fluorine-doped tin oxide (FTO) glasses ($10\text{--}15 \Omega \text{sq}^{-1}$) were ultrasonically cleaned in acetone, ethanol, distilled water for 10 min each, and dried under nitrogen flow before further experimentation. In a typical hydrothermal synthesis of TiO_2 , a 1 ml solution of titanium butoxide was added to the well-mixed solution of 30 ml distilled water and 30 ml concentrated HCl (Junsei, 35–37%), and the resulting solution was stirred for 30 min. This resulting solution was transferred into a Teflon-lined stainless steel

autoclave containing two FTO glass substrates mounted to the FTO holder. The autoclave was then closed and maintained at 150 °C for 4 h. After completion of the reaction, the white TiO₂/FTO films were rinsed with deionized water and dried in air.

Hydrothermal synthesis of ZnIn₂S₄ on TiO₂/FTO glass was prepared by a simple method as reported by Peng et al. [21]. In this process, ZnSO₄·7H₂O (1.6 mmol), InCl₃·4H₂O (3.2 mmol), and C₂H₅NS (6.4 mmol) were added to 50 ml of distilled water and stirred for 30 min. The solution was then transferred into a Teflon-lined stainless steel autoclave containing TiO₂/FTO substrates. The autoclave was filled up to 60% capacity, sealed, maintained at 160 °C for 2 h, and cooled naturally to room temperature. The samples were rinsed with ethanol and dried at room temperature. The ZnIn₂S₄ film deposited on TiO₂/FTO was yellowish in color. As shown in Fig. 1, a layer of metal oxide (TiO₂, Al₂O₃, SiO₂) was coated on the ZT/FTO by dipping the films in the appropriate amount of (10 μM) titanium isopropoxide (C₁₂H₂₈O₄Ti), aluminium iso-

propoxide (C₉H₂₁O₃Al), and tetraethyl orthosilicate (SiC₈H₂₀O₄) solutions for 2 min and drying in air for 20 min. Furthermore, the annealing of TiO₂, Al₂O₃, and SiO₂-coated ZT films was performed at 200 °C for 30 min to improve the film quality; the corresponding photoanodes were labeled as TZT, AZT and SZT, respectively, and were subjected to further characterizations.

2.3. PEC measurements

All photoelectrochemical experiments were conducted in a three-electrode system with the metal oxide coated ZT as the working electrode, Pt wire as the counter electrode, and Ag/AgCl as the reference electrode, using an approach as in an earlier work [22]. The photocurrent-voltage (J-V) curves, electrochemical impedance spectroscopy (EIS), and Mott-Schottky (M-S) studies were performed using a portable potentiostat (COMPACTSTAT.e, Ivium, Netherland) equipped with an electrochemical interface and

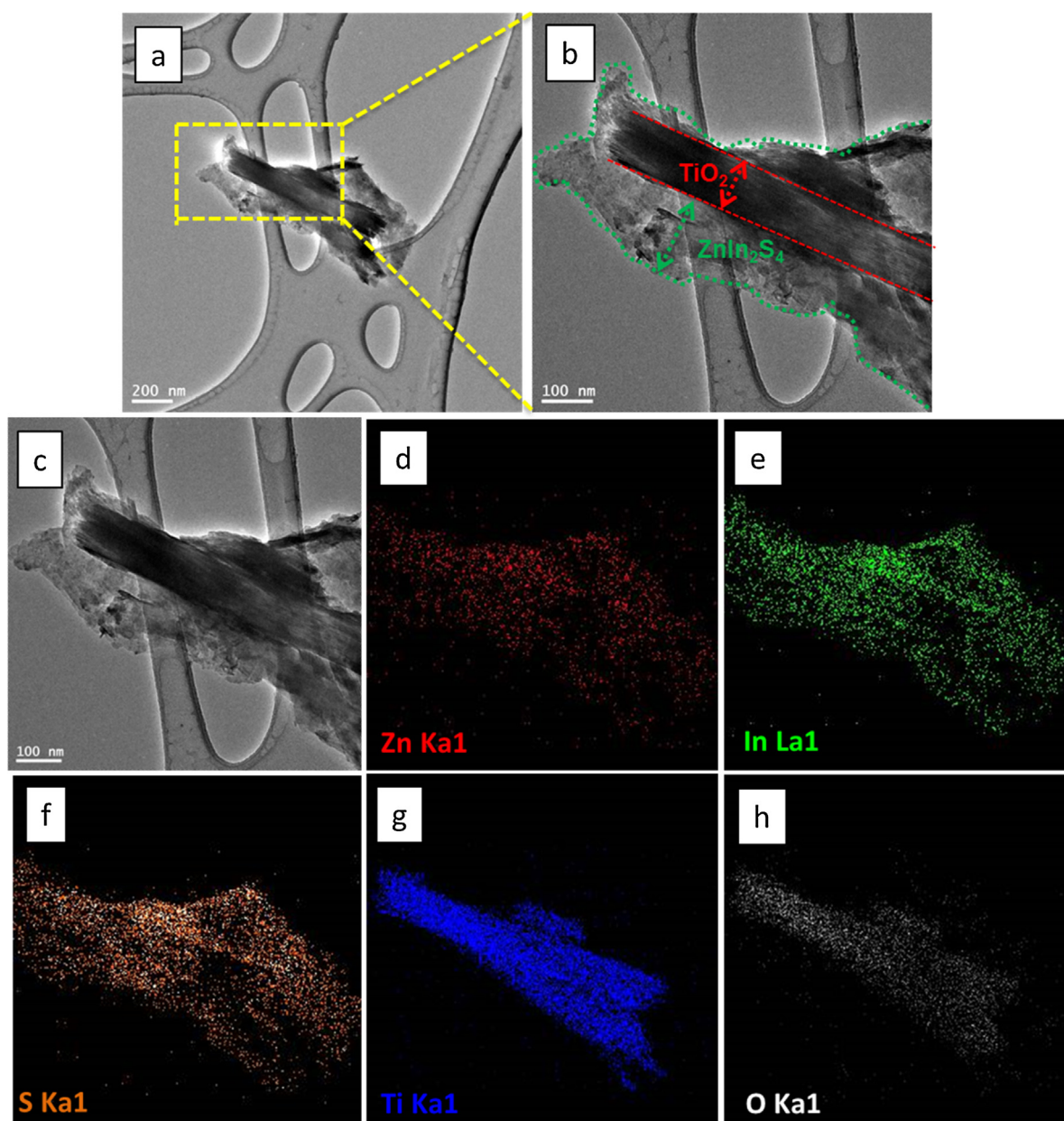


Fig. 4. (a, b) TEM image of the ZT photoelectrode, (c) EDS mapping of the selected TEM image area with corresponding elemental mapping images for (d) Zn, (e) In, (f) S, (g) Ti, and (h) O.

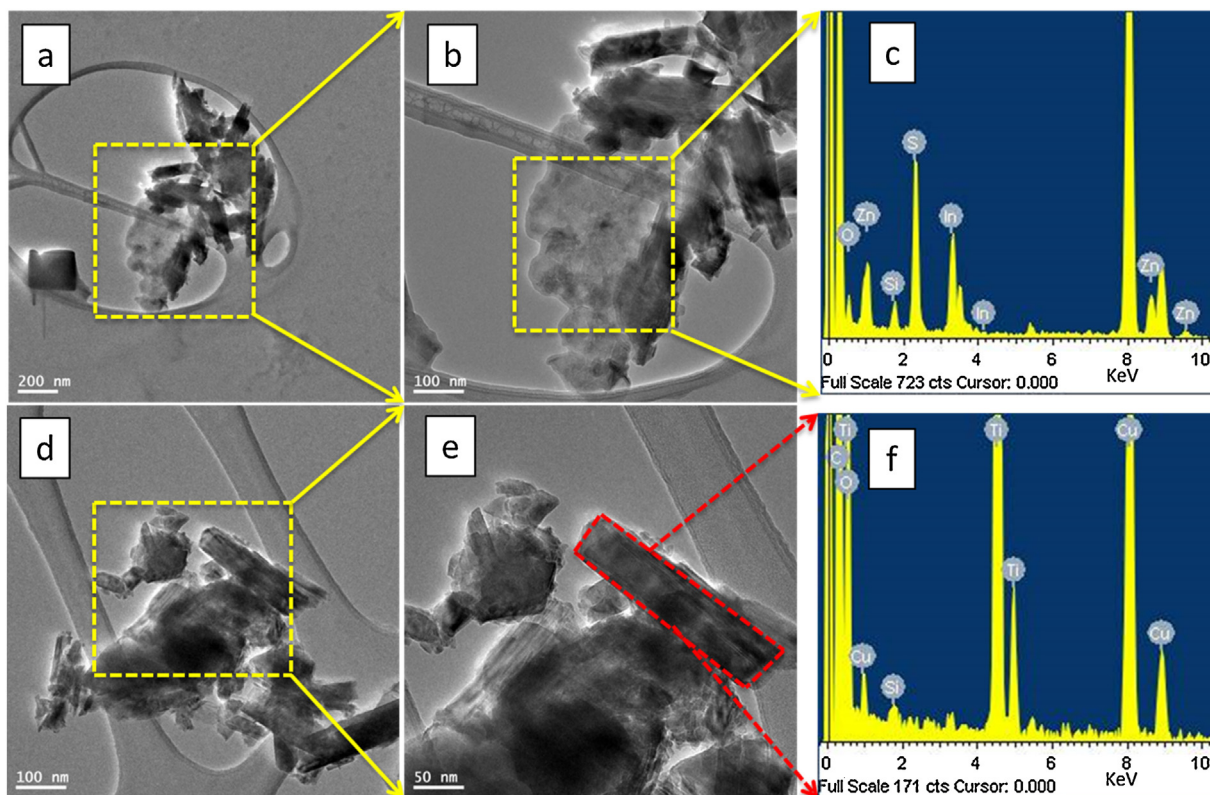


Fig. 5. (a, b, d and e) TEM images and (c and f) EDS images of the SZT electrodes.

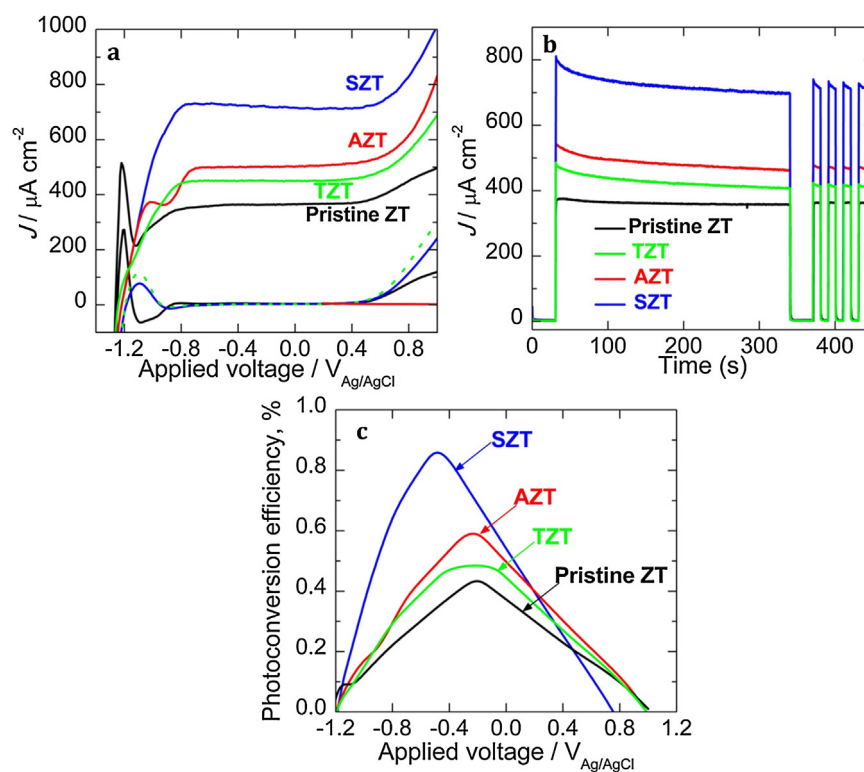


Fig. 6. (a) Photocurrent potential characteristics, and (b) long term photostability and transient photocurrent responses at 0.1 V vs. Ag/AgCl, (c) corresponding photoconversion efficiency of ZT, TZT, AZT, and SZT photoelectrodes in a 0.1 M Na_2S + 0.02 M Na_2SO_3 electrolyte.

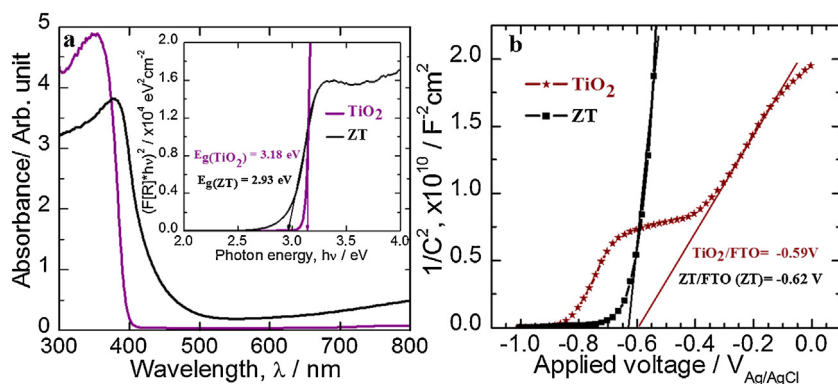


Fig. 7. (a) UV-vis absorbance and Tauc plots, (b) Mott-Schottky plots of the pristine TiO₂ and ZT photoelectrodes.

Table 1

Parameters determined from EIS fitting of metal oxide coated ZT photoelectrodes.

Samples/ parameters	R_s (Ω)	R_{ct} (Ω)	$C_{[CPE]}$ (μF)	W_s (Ω)
ZT	24.42	4723	5.969	183.1
TZT	34.26	1075	9.133	13.8
AZT	26.79	548	8.066	16.3
SZT	27.19	435	5.247	16.1

impedance analyzer facility. The EIS measurement was performed at 0.1 V vs. Ag/AgCl with an AC perturbation amplitude of 10 mV, in the frequency range of 100 kHz to 0.1 Hz, and under a simulated one sun illumination (100 mW cm^{-2}) using a solar simulator (Abet Technologies). The electrolyte consisted of 0.1 M Na₂S and 0.02 M Na₂SO₃ in deionized water. The experimental EIS data was validated using the Kramers-Kronig transform test and then fitted to the suitable equivalent circuit model using the ZView (Scribner Associates Inc.) program.

2.4. Photoelectrochemical hydrogen production

The photoelectrochemical hydrogen production experiment was performed in a closed reactor with SZT/FTO thin film as the photoanode, a Pt counter electrode, and Ag/AgCl as the reference electrode. A simulated one sun illumination (100 mW cm^{-2}) was used to perform photoelectrochemical hydrogen production in an aqueous electrolyte consisting of 0.1 M Na₂S and 0.02 M Na₂SO₃. All experiments were performed at a 0.1 V bias (vs. Ag/AgCl). Evolved hydrogen was analysed with a gas chromatography with a TCD using a 5-Å molecular sieve column and N₂ as the carrier gas.

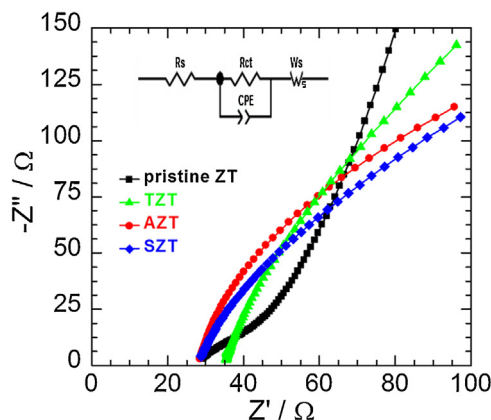


Fig. 8. Nyquist plots of ZT, TZT, AZT, and SZT photoelectrodes in a 0.1 M Na₂S + 0.02 M Na₂SO₃ electrolyte. The inset depicts the equivalent circuit model used for fitting.

2.5. Characterization of TiO₂, Al₂O₃, and SiO₂-coated ZT heterostructure photoelectrodes

The X-ray diffraction analysis of deposited metal oxide coated ZT was performed using a PANalytical X'pert Pro diffractometer equipped with a Cu K α radiation source (wavelength $\lambda = 1.540598 \text{ \AA}$ and $\lambda = 1.544426 \text{ \AA}$) in the range of 20–80° and recorded at a scan rate of $0.02^\circ \text{ s}^{-1}$. X-ray photoelectron spectroscopy (XPS, Thermo Scientific XPS spectrometer) equipped with a monochromatic Al K α X-ray source ($h\nu = 1486.6 \text{ eV}$) was used to study the valence state and elemental quantification of films. The morphological studies of the deposited films were examined using a field emission scanning electron microscope (FESEM) (SUPRA 40VP, Carl Zeiss, Germany) equipped with an X-ray energy dispersive spectrometer (EDX). Transmission electron microscopy (TEM) was performed with a JEOL JEM-3100F transmission electron microscope operating at 200 kV. The sample for TEM was prepared by placing a drop of the sample suspension in ethanol on a standard carbon-coated copper grid. A UV-vis diffuse reflectance spectroscopy study was performed using a dual-beam spectrophotometer (Shimadzu, UV-2600 series) in the wavelength range of 300–800 nm.

3. Results and discussion

Fig. S1 shows the XRD patterns of TiO₂, ZT, TZT, AZT, and SZT. After subtracting the diffraction peaks of FTO from the XRD pattern of ZT, other diffraction peaks were indexed to the characteristic peaks of tetragonal rutile TiO₂ (JCPDS No. 76-1940) and the hexagonal phase of ZnIn₂S₄ (JCPDS card No. 65-2023), confirming that the ZnIn₂S₄ layer is present on rutile TiO₂ nanorods. The metal oxide (MO=TiO₂, Al₂O₃, SiO₂) layer coated ZT samples exhibited a similar XRD patterns as pristine ZT. However, the intensity of the XRD spectrum was significantly suppressed, particularly for the diffraction peaks of rutile TiO₂ and ZnIn₂S₄ in the case of TZT, AZT, and SZT. This confirms the presence of TiO₂, Al₂O₃, and SiO₂ layers on the ZT thin films. Peaks corresponding to Al₂O₃ and SiO₂ were not observed in the XRD patterns. To confirm the elemental composition and valence states, the TZT, AZT, and SZT samples were characterized by XPS. XPS survey scan measurements (Fig. S2a) show that the chemical binding energies (BE's) for Ti2s, Ti2p, O1s, Zn2p, In3d, S2p, and C1s are 565.4, 458.4, 529.4, 1023, 1045.5, 445.5, and 284.6 eV, respectively, indicating that the films contained predominantly Ti, O, Zn, In, S, and C elements. The C1s peak may be caused by the C element from the measured environment or the remnant organic precursors that were not completely removed during the hydrothermal process [23]. Fig. 2(a–d) shows the high-resolution XPS spectra of Ti2p, Al2p, Si2p, and O1s, respectively, for TZT, AZT, and SZT. Ti2p spin-orbit components (2p_{3/2} and 2p_{1/2})

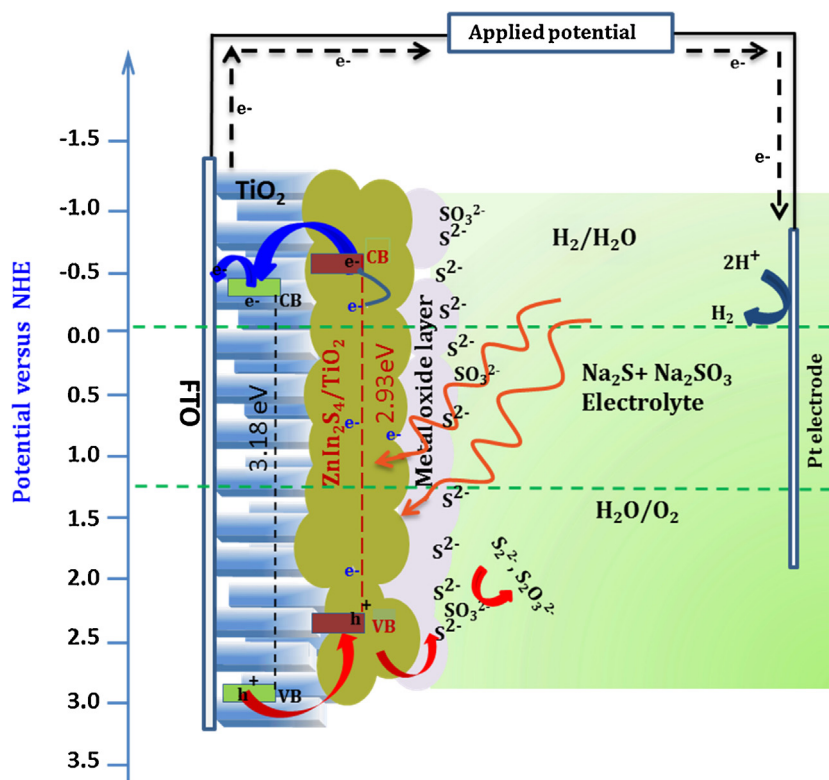


Fig. 9. Schematic of charge transfer mechanism in metal oxide coated ZT photoanode.

were observed at 458.40 and 464.50 eV. The calculated BE difference between the Ti 2p_{3/2} and Ti 2p_{1/2} peaks was 5.7 eV, which is consistent with the BE separation observed for stoichiometric TiO₂ [24]. In the AZT sample, the symmetric Al2p signal was near 74.8 eV, which indicates the formation of γ -Al₂O₃ [25]. However the high resolution XPS peaks of Al 2p and O1s were centered at 74.8 and 531.52 eV, respectively, with a O1s–Al2p BE difference of 456.72 eV, which is consistent with fully oxidized O–Al–O bonding [26]. The high-resolution XPS spectra (Fig. 2c) do not show a Si2p peak in the SZT, which may be due to the low Si content or non-uniform distribution of SiO₂ on the ZT surface. Furthermore, in the case of SZT, a very small XPS peak of O1s was observed confirming a small amount of SiO₂ on ZT. The broadened O1s peak in TZT and AZT can be assigned to the peak of lattice oxygen and surface hydroxyl groups, or chemisorbed water molecules on the film surface [27]. The shift in the binding energies of O1s in metal oxide/ZT as compared to the corresponding transition-metal oxides (TM–O oxides) reported in the literature (i.e., TiO₂ [28], Al₂O₃ [29], and SiO₂ [30]) is a result of the fact that the metal–S bonds in the metal oxide layer coated ZT samples are weaker than oxides, as sulfur is much less electronegative than oxygen. These results also confirm that the metal oxides are spread on the ZT and form bonds with sulfur. High-resolution XPS spectra of Zn2p, In3d, and S2p [Fig. S2 (b–c)] for metal oxide coated ZT indicated characteristic binding energies of 1045.8 eV for Zn 2p_{1/2}, 1023 eV for Zn 2p_{3/2}, 445.8 eV for In 3d_{5/2}, and 453.4 eV for In 3d_{3/2}. As seen in Fig. S2d, the broad and intense asymmetric XPS peak of S2p in SZT compared to that of TZT and AZT were observed at 161.8 eV, which indicated a very thin layer of SiO₂ compared to the Al₂O₃ and TiO₂ layers. However, the binding energy values were very close to those previously reported [31,32], indicating that the valence states of Zn, In, and S are 2+, 3+, and 2–, respectively.

Fig. S3a shows the field emission scanning electron microscopy (FESEM) image of the hydrothermally-prepared TiO₂ nanorod arrays. The entire surface of the FTO substrate was covered with

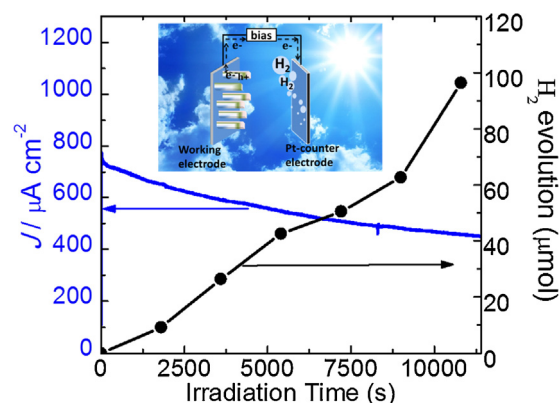


Fig. 10. Evolution of H₂ and photocurrent density as a function of time measured at 0.1 V vs. Ag/AgCl using SZT as a photoelectrode under 100 mW cm^{−2} light illumination in a three-electrode configuration, Inset shows a schematic of the photoelectrochemical hydrogen generation.

uniformly and densely packed, vertically-aligned TiO₂ nanorods. The top facets of the nanorods were square, suggesting an expected growth pattern of a tetragonal crystal structure on the FTO substrate. Fig. S3b indicates that ZnIn₂S₄ forms a continuous layer nanosheet on the top surface of the TiO₂ nanorod array with an enhanced surface area of the photoelectrode. The cross-sectional view of the ZT film (Fig. S3c) reveals that ZnIn₂S₄ nanosheets are present on the TiO₂ surface and also inserted in the voids among the TiO₂ nanorods. Fig. 3 shows the top and cross-sectional FESEM views of the metal oxide (TiO₂, Al₂O₃ and SiO₂) layer coated ZT thin films. After the metal oxide coating, the morphology of the ZT thin film changed remarkably, indicating a thin coating of the metal oxide layer on the ZnIn₂S₄ nanosheet. The gap between the nanosheets of ZnIn₂S₄ decreased in the TZT and SZT samples with the formation of a net-like structure after the metal oxide coating.

This change in the surface morphology of ZT after the metal oxide coatings may be responsible for the providing more surface area of electrode coming in contact with electrolyte, more scattering of light and hence, the enhanced absorption of the film. The element composition of the metal oxide layer-coated ZT photoanodes was further characterized using energy dispersive spectrometer (EDS) mapping and is shown in Figs. S4(a,b). EDS mapping of TZT illustrates that both elemental Ti and O were uniformly distributed over the ZT surface, producing a uniform layer of TiO_2 over the entire ZnIn_2S_4 nanosheet morphology. In the case of AZT thin films, Al and O cover the whole surface of the ZT film. To study the crystalline structure of the ZT photoelectrode after the SiO_2 layer, TEM was performed for the ZT and SZT photoelectrodes. The sample specimen for TEM analysis was obtained by scratching the ZT and SZT films from the FTO glass. Fig. 4(a,b) shows the TEM image of the hydrothermally-prepared pristine ZT thin films, demonstrating the presence of a ZnIn_2S_4 nanosheet on the surface of the TiO_2 nanorod. In addition, Fig. 4(c–h) shows the selected area for elemental mapping of Zn, In, S, Ti, and O, further confirming the coexistence of ZnIn_2S_4 and TiO_2 in the ZT. The chemical composition of ZT was also supported by EDS analysis as shown in Fig. 4S(c), and the ZT heterostructure consisted of zinc, indium, sulphur, titanium, and oxygen, with a molar ratio of zinc, indium, and sulfur of 1:2:4. However, the TEM images of the SZT electrode indicated the presence of only the ZnIn_2S_4 nanosheet in Fig. 5(a–b) and TiO_2 nanorods in Fig. 5(d–e). Although a SiO_2 layer was not observed distinctly in the TEM image, the existence of Si and Ti in the energy-dispersive X-ray spectrometry (EDS) analysis (Fig. 5c and f, respectively) suggests that SiO_2 may exist in the amorphous state. A remarkably low Si content (i.e., 0.68%) was observed on the surface of ZT. These results are consistent with the XPS result of SZT. The amorphous SiO_2 coating on the ZT heterostructure may help for trapping the maximum absorbed light and facilitating the interfacial charge transport in enhancing the photocurrent in the metal oxide layer coated ZT heterojunction photoanode.

UV–vis diffuse reflectance (DRS) spectra were used to study the optical properties of TZT, AZT, and SZT samples. Fig. S5a shows the absorption spectra of the samples determined using the Kubelka–Munk function [33], $F(R) = (1-R)^2/2R = k/s$, where, R is the reflectance, k is the Kubelka–Munk absorption, and s is the scattering coefficient. Fig. S5b shows the band gap energies of ZT-based thin films. The TZT, AZT, and SZT samples show a slight red-shift of the absorption edges, confirming that the band gap of ZT gradually decreases with the metal oxide coating. The band gap energy of the SZT photoanode lies between that of TZT and AZT. Despite this, a higher photoactivity for SZT than that of TZT and AZT photoanodes could be ascribed to the SiO_2 coating that causes relatively higher surface passivation in ZT than in TiO_2 and Al_2O_3 . In the semiconductor, photoactivity is a function of the lifetime and trapping rate of photogenerated electrons and holes.

To evaluate influence of the metal oxide on ZT thin films, the photoelectrochemical performance was studied using a three-electrode system. Fig. 6a shows the photocurrent density–potential curves of pristine ZT, TZT, AZT, and SZT recorded under one sun illumination and dark conditions in the 0.1 M $\text{Na}_2\text{S} + 0.02$ M Na_2SO_3 electrolyte. Under dark conditions, all ZT-based film shows a small current density of approximately 5.8 nA cm^{-2} ; under illumination, all photocurrents showed outstanding enhancements compared to the dark currents due to the light response of the electrodes. However, the photocurrent density of the SZT film was approximately 0.786 mA cm^{-2} , which is two times greater than that of pristine ZT (0.370 mA cm^{-2}) and more than 1.5 times greater than that of TZT and AZT. Fig. 6b shows the long-term photostability and transient photocurrent responses for 430 s of pristine ZT, TZT, AZT, and SZT photoanodes at 0.1 V vs. Ag/AgCl, before the photocurrent density–potential curve measurements. The photo-conversion

efficiency of metal oxide-coated ZT films was calculated using an equation reported by Khan et al. [34] and is shown in Fig. 6c. The photo-conversion efficiencies of 0.46, 0.56, 0.62, and 0.9%, were obtained for pristine ZT, TZT, AZT, and SZT photo-electrodes, respectively, at 0.1 V vs. Ag/AgCl under one sun illumination. The increase in photocurrent density and photo-conversion efficiency of SZT could be attributed to the decrease in electron-hole recombination and charge transfer resistance.

Further to illustrate the corresponding charge transfer mechanism in metal oxide coated ZT, the optical absorbance and flat band potential (V_{fb}) of pure TiO_2 and the ZT heterostructures were determined by a UV–vis diffuse reflectance spectra (DRS) and Mott–Schottky (M–S) analysis. As shown in Fig. 7(a), absorption wavelength in ZT shifted above 425 nm, suggesting an increased absorption compared to that of pure TiO_2 (band gap 3.18 eV). To ascertain the position of band edges of ZT and TiO_2 , the hydrothermally-prepared TiO_2 nanorod photo-electrodes with and without ZnIn_2S_4 were investigated via a M–S analysis. In photo-electrochemistry, the measurement of the V_{fb} is a very useful quantity, as it shows the energetic position of the valence and conduction band edge of a given semiconductor material [35,36]. The V_{fb} could be calculated by extrapolating the linear region in the M–S plots ($1/C^2$ vs. V) as shown in Fig. 7b. There was a small shift in the V_{fb} towards a negative value that suggested a higher carrier concentration and efficient charge transfer in the case of ZT compared to TiO_2 [37]. However, in a potential range of -0.90 to -0.39 V vs. Ag/AgCl, a nonlinear M–S behavior was observed for the as-prepared TiO_2 electrode, which is attributed to a deep-surface state in the band gap [38] that is in agreement with previously reported TiO_2 behavior [39].

The generation of electron/hole pairs, as well as their separation, and migration, is identified as one of most important fundamental stage for the photocatalysts. Generally in semiconductors, photocurrent depends on electron generation, charge-recombination, and charge transfer processes [40]. Therefore, to further elucidate the photoelectrocatalytic activity, the charge transfer characteristics of the ZT photoanodes with respect to the surface coatings of metal oxides, such as TiO_2 , Al_2O_3 , and SiO_2 , were studied using EIS. Fig. 8 shows the Nyquist plots (Z' vs. $-Z''$) of pristine ZT and metal oxide-coated TZT, AZT, and SZT photoanodes. The plots were fitted and modelled using a Randles equivalent circuit [41]. The equivalent circuit elements in the fit include a series resistance (R_s), a charge transfer resistance from the surface to solution (R_{ct}), a capacitance (C_{PE} , a constant phase element for imperfect capacitance), and Nernst diffusion impedance (W_s) of the electrolyte in the pores of the electrode material. These parameters were determined by fitting the impedance spectra (Table 1), and good agreement between the measured and fitted data was achieved in all cases. Smaller R_{ct} values led to greater separation efficiency of the photo-generated electron–hole pairs [42,43]. The R_{ct} value of photoanodes decreased noticeably in the order: $\text{SZT} < \text{AZT} < \text{TZT} < \text{ZT}$, as shown in Table 1. The EIS results are concurrent with the photocurrent measurements, which suggest that thin metal oxide layers passivate the surface defects and suppress the charge recombination. Among the studied coatings, SiO_2 is the best choice in improving the interface properties of the ZT photoanode that lead to efficient separation of charge carriers. The photocatalytic activity of photocatalysts can greatly influence the surface morphology [44] and bandgap. In the present study, metal oxide coated ZT electrodes show nearly the same absorption spectra, which indicated that the band structure or band gap did not contribute much to the enhanced photocatalytic activity. Therefore, there must be some other key factors, such as the surface treatment, to influence the charge separation efficiency and thereby increase the photocatalytic activity of the metal oxide coated ZT.

In the present case of metal oxide coated ZT samples, the recombination reaction of injected photoelectrons with the oxidizing agent of the electrolyte can only be finished by tunnelling through a layer of metal oxide (i.e., TiO_2 , Al_2O_3 , SiO_2). Therefore, the deposited metal oxide acts as a barrier for the interfacial electron transfer, suppressing recombination and to increase the photocurrent [45]. The expected working mechanisms for enhanced photocatalytic activities of metal oxide coated ZT using obtained band gap and V_{fb} values of TiO_2 and ZT are shown in Fig. 9. In the case of the metal oxide coated ZT photoelectrode, TiO_2 acts as the electron acceptor, and the Fermi levels of TiO_2 and ZnIn_2S_4 are aligned at the equilibrium condition. The potential difference of the conduction band edge of ZnIn_2S_4 and TiO_2 produces a built-in electric field and concentration gradient. The difference in the flat band potential of ZT and TiO_2 transfers the photo-generated electrons from the conduction band (CB) of ZnIn_2S_4 to that of TiO_2 ; then, the electrons migrate to the surface of the counter electrode where they can reduce H^+ to hydrogen. Alternatively, because of more positive valance band (VB) edge of TiO_2 than that of ZnIn_2S_4 , the holes in the VB of the TiO_2 transfer to ZnIn_2S_4 and react with the SO_3^{2-} , S^{2-} ions in the electrolyte and produces the S_2^{2-} and $\text{S}_2\text{O}_3^{2-}$ [17]. Thus, photo-generated charge carries (e.g., electrons and holes) are effectively separated at the ZT interface and the recombination is inhibited to a certain extent. However, due to the defects and imperfections, there is risk of interface recombination that limits the photocatalytic activity. In order to reduce the recombination losses in the ZT photoanodes, a metal oxide was coated onto the ZT. In such cases, the metal oxides can minimize the interface recombination losses and help to attain large band-bending that improves the charge transport efficiency at the electrode-electrolyte interface. The main function of the metal oxide layer is to retard interfacial charge recombination [46]. With the metal oxide coating in our study, the photocatalytic efficiency of the ZT photocatalysts was improved, which can be attributed to (i) the fast separation of the photoinduced electron/hole pairs and (ii) the minimization of the recombination losses at the junctions [47]. The relatively higher photocurrent in SZT is attributed to the distribution of SiO_2 on ZT should enhance the charge transfer and reduce the recombination losses at the surface of ZT compared to that of TiO_2 .

Since higher photoelectrochemical performance was observed for the SZT electrode, we further studied the photoelectrocatalytic hydrogen generation using SZT at a 0.1 V bias (vs. Ag/AgCl) in an electrolyte consisting of a 0.1 M Na_2S and 0.02 M Na_2SO_3 solution under one sun illumination. Fig. 10 shows the photoelectrocatalytic hydrogen evolution over the SZT photocathode analyzed by gas chromatography (GC) and photocurrent density with respect to time. Schematic of the simple photoelectrochemical hydrogen generation is shown in the inset of

Fig. 10. The hydrogen evolution linearly increased with the solar light irradiation time, and the total amount of H_2 produced by SZT was $96 \mu\text{mol}$ after 3 h ($32 \mu\text{mol h}^{-1}$). The photostability of the photoanode was also investigated during the hydrogen production. Although relatively good photocurrent enhancement was observed for ZT after SiO_2 surface treatment, the SZT electrode suffers from low photocurrent stability. After 3 h, the decay of the SZT photoanode current density seems to be primarily caused by the photo-corrosion upon illumination during hydrogen production. Such corrosion might be possible because of photogenerated holes participating in the surface oxidation. The surface oxidation cannot be avoided with a thin SiO_2 layer on the ZT electrodes; however, surface modification with a higher band gap material such as SiO_2 acts as a passivation layer. Therefore, the thickness, effect of thermal treatment of the SiO_2 layer should be optimized in future work in order to modify the synthesized ZT photoelectrode and further improve the photocurrent and photostability.

4. Conclusions

In summary, metal oxide (TiO_2 , Al_2O_3 , SiO_2)-coated ZT heterostructures were fabricated on the FTO substrate via a facile hydrothermal and effective dip-coating method. The metal oxide top layer coating on the ZT photoanode improved the photoelectrochemical performance. The photocurrent density of SZT ($\sim 0.786 \text{ mA cm}^{-2}$) was two-folds greater than that of pristine ZT at 0.1 V vs. Ag/AgCl. The corresponding in situ photoelectrochemical hydrogen production rate for the SZT photoanode was $32 \mu\text{mol h}^{-1}$. This work demonstrates that the surface treatment of SiO_2 simultaneously enhances the interfacial charge transfer by reducing the recombination losses of the charge carriers. The results provide useful insights for developing a new strategy for sulfide or chalcogenide-based nanoarchitectures in photoelectrochemical hydrogen generation.

Acknowledgments

This research was supported by the Basic Science Research Programs through the National Research Foundation of Korea (NRF), funded by the Ministry of Education, Science and Technology (2012R1A6A3A04038530), as well as the Korea Ministry of Environment (MOE) as Public Technology Program based on Environmental Policy (2014000160001).

Appendix A. Supplementary data

Supplementary data associated with this article can be found, in the online version, at <http://dx.doi.org/10.1016/j.apcatb.2015.12.001>.

References

- [1] Y. Ma, X. Wang, Y. Jia, X. Chen, Hongxian Han, Can Li, *Chem. Rev.* 114 (2014) 9987–10043.
- [2] A. Kubacka, M. Fernandez-Garcia, G. Colon, *Chem. Rev.* 112 (2012) 1555–1614.
- [3] A. Fujishima, K. Honda, *Nature* 238 (1972) 37–38.
- [4] H.X. Li, Z.F. Bian, J. Zhu, D.Q. Zhang, G.S. Li, Y.N. Huo, H. Li, Y.F. Lu, *J. Am. Chem. Soc.* 129 (2007) 8406–8407.
- [5] J.J. Zou, C.J. Liu, *Acta Phys. Chim. Sin.* 22 (2006) 926–931.
- [6] K. Pan, Y. Dong, W. Zhou, Q. Pan, Y. Xie, T. Xie, G. Tian, G. Wang, *ACS Appl. Mater. Interfaces* 5 (2013) 8314–8320.
- [7] J.H. Kim, T.K. Yun, J.Y. Bae, K.S. Ahn, *Jpn. J. Appl. Phys.* 48 (2009) 1202041–1202043.
- [8] J.F. Lei, L.B. Li, X.H. Shen, K. Du, J. Ni, C.J. Liu, W.S. Li, *Langmuir* 29 (2013) 13975–13981.
- [9] Z. Jiao, T. Chen, H. Yu, T. Wang, G. Lu, Y. Bi, *J. Colloid Interface Sci.* 419 (2014) 95–101.
- [10] J. Luo, L. Ma, T. He, C.F. Ng, S. Wang, H. Sun, H.J. Fan, *J. Phys. Chem. C* (2012) 11956–11963.
- [11] N. Serpone, P. Maruthamuthu, P. Pichat, E. Pelizzetti, H. Hidaka, *J. Photochem. Photobiol. A* 85 (1995) 247–255.
- [12] S. Peng, L. Li, Y. Wu, L. Jia, L.L. Tian, M. Srinivasan, S. Ramakrishna, Q. Yan, S.G. Mhaisalkar, *Cryst. Eng. Comm.* 15 (2013) 1922–1930.
- [13] N.S. Chaudhari, A.P. Bhirud, R.S. Sonawane, L.K. Nikam, S.S. Warule, V.H. Rane, B.B. Kale, *Green Chem.* 13 (2011) 2500–2506.
- [14] S.H. Shen, L. Zhao, Z.H. Zhou, L.J. Guo, *J. Phys. Chem. C* 112 (2008) 16148–16155.
- [15] Q. Liu, H. Lu, Z. Shi, F. Wu, J. Guo, K. Deng, L. Li, *ACS Appl. Mater. Interfaces* 6 (2014) 17200–17207.
- [16] F.M. Pesci, A.J. Cowan, B.D. Alexander, J.R. Durrant, D.R. Klug, *J. Phys. Chem. Lett.* 2 (2011) 1900–1903.
- [17] W. Kim, T. Tachikawa, D. Monllor-Satoca, H. Kim, T. Majim, W. Choi, *Energy Environ. Sci.* 6 (2013) 3732–3739.
- [18] F.L. Forman, N. Tetreault, M. Cornuz, T. Moehl, M. Grätzel, K. Sivula, *Chem. Sci.* 2 (2011) 737–743.
- [19] H. Yan, J. Yang, G. Ma, G. Wu, X. Zong, Z. Lei, J. Shi, C. Li, *J. Catal.* 266 (2009) 165–168.
- [20] E.S. Aydil, B.J. Liu, *J. Am. Chem. Soc.* 131 (2009) 3985–3990.
- [21] S. Peng, P. Zhu, V. Thavasi, S.G. Mhaisalkar, S. Ramakrishna, *Nanoscale* 3 (2011) 2602–2608.
- [22] P.S. Shinde, A. Annamalai, J.H. Kim, S.H. Choi, J.S. Lee, J.S. Jang, *Sol. Energy Mater. Sol. Cells* 141 (2015) 71–79.

- [23] J. Zhou, F. Ren, S. Zhang, W. Wu, X. Xiao, Y. Liu, C. Jiang, *J. Mater. Chem. A* 1 (2013) 13128–13138.
- [24] M.N. Ghazzal, N. Chaoui, M. Genet, E.M. Gaigneaux, D. Robert, *Thin Solid Films* 520 (2011) 1147–1154.
- [25] L. Nie, A. Meng, J. Yu, M. Jaroniec, *Sci. Rep.* 3 (2013) 32151–32156.
- [26] B. Lee, S.Y. Park, H.C. Kim, K. Cho, E.M. Vogel, M.J. Kim, R.M. Wallace, J. Kim, *Appl. Phys. Lett.* 92 (2008) 2031021–2031023.
- [27] K. Nagaveni, M.S. Hegde, N. Ravishankar, G.N. Subbanna, G. Madras, *Langmuir* 20 (2004) 2900–2907.
- [28] C. Su, L. Liu, M. Zhang, Y. Zhang, C. Shao, *Cryst. Eng. Comm.* 14 (2012) 3989–3999.
- [29] O. Renault, L.G. Gosset, D. Rouchon, A. Ermoloeff, *J. Vac. Sci. Technol. A* 20 (2002) 1867–1876.
- [30] E.G. Barbagiovanni, L.V. Goncharova, P.J. Simpson, *Phys. Rev. B* 83 (2011) 03511201–03511211.
- [31] L. Ye, J. Fu, Z. Xu, R. Yuan, Z. Li, *ACS Appl. Mater. Interfaces* 12 (2014) 3483–3490.
- [32] J. Hou, C. Yang, H. Cheng, Z. Wang, S. Jiao, H. Zhu, *Phys. Chem. Chem. Phys.* 15 (2013) 15660–15668.
- [33] A. Mahyar, M.A. Behnajady, N. Modirshahla, *Indian J. Chem. A* 49 (2010) 1593–1600.
- [34] S.U.M. Khan, M. Al-Shahry, W.B. Ingler Jr., *Science* 297 (2002) 2243–2245.
- [35] M. Gratzel, *Nature* 414 (2001) 338–344.
- [36] P. Xiang, X. Li, H. Wang, G. Liu, T. Shu, Z. Zhou, Z. Ku, Y. Rong, M. Xu, L. Liu, M. Hu, Y. Yang, W. Chen, T. Liu, M. Zhang, H. Han, *Nanoscale Res. Lett.* 6 (2011) 6061–6065.
- [37] U. Bach, D. Lupo, P. Comte, J.E. Moser, F. Weissörte, J. Salbeck, H. Spreitzer, M. Grätzel, *Nature* 395 (1998) 583–585.
- [38] S. Takata, Y. Miura, Y. Matsumoto, *Phys. Chem. Chem. Phys.* 16 (2014) 24784–24789.
- [39] W. Siripala, M. Tomkiewicz, *J. Electrochem. Soc.* 128 (1981) 2491–2492.
- [40] L. Long, L. Wu, X. Yang, X. Li, *J. Mater. Sci. Technol.* 30 (2014) 765–769.
- [41] B. Klahr, S. Gimenez, F. Fabregat-Santiago, T. Hamann, J. Bisquert, *J. Am. Chem. Soc.* 134 (2012) 4294–4302.
- [42] M.A. Mahadik, P.S. Shinde, M. Cho, J.S. Jang, *J. Mater. Chem. A* 3 (2015) 23597–23606.
- [43] M.L. Chang, L.P. Wu, X.J. Li, W. Xu, *J. Mater. Sci. Technol.* 28 (2012) 594–598.
- [44] I.A. Howard, R. Mauer, M. Meister, F. Laquai, *J. Am. Chem. Soc.* 132 (2010) 14866–14876.
- [45] X. Gao, D. Guan, J. Huo, J. Chen, C. Yuan, *Nanoscale* 5 (2013) 10438–10446.
- [46] E. Palomares, J.N. Clifford, S.A. Haque, T. Lutz, J.R. Durrant, *J. Am. Chem. Soc.* 125 (2003) 475–482.
- [47] S. Yang, L. Li, W. Yuan, Z. Xia, *Dalton Trans.* 44 (2015) 6374–6383.